
Quantization-based Bounds on the Wasserstein Metric

Jonathan Bobrutsky

Department of Statistics and Operations Research
Tel Aviv University
jbobrutsky@gmail.com

Amit Moscovich

Department of Statistics and Operations Research
Tel Aviv University
mosco@tauex.tau.ac.il

Abstract

The Wasserstein metric has become increasingly important in many machine learning applications such as generative modeling, image retrieval and domain adaptation. Despite its appeal, it is often too costly to compute. This has motivated approximation methods like entropy-regularized optimal transport, downsampling, and subsampling, which trade accuracy for computational efficiency. In this paper, we consider the challenge of computing efficient approximations to the Wasserstein metric that also serve as strict upper or lower bounds. Focusing on discrete measures on regular grids, our approach involves formulating and exactly solving a Kantorovich problem on a coarse grid using a quantized measure and specially designed cost matrix, followed by an upscaling and correction stage. This is done either in the primal or dual space to obtain valid upper and lower bounds on the Wasserstein metric of the full-resolution inputs. We evaluate our methods on the DOTmark optimal transport images benchmark, demonstrating a 10x–100x speedup compared to entropy-regularized OT while keeping the approximation error below 2%.

1 Introduction

The Wasserstein metric is a basic tool in machine learning with widespread adoption in various domains, including computer vision, natural language processing, and computational biology [Arjovsky et al., 2017, Kusner et al., 2015, Schiebinger et al., 2019]. While it is fast to compute in particular cases, such as one-dimensional distributions, in general settings computing the Wasserstein metric can be very expensive. For example, consider the calculation of the Wasserstein metric between $N \times N$ images that we treat as discrete measures on a regular grid. Each image has N^2 pixels, so computing the Wasserstein metric involves solving a linear program with $N^2 \times N^2$ variables and $\Theta(N^2)$ constraints. This is typically done using a network simplex algorithm whose worst-case runtime in this case is $O(N^6 \log N)$ [Peyré and Cuturi, 2019]. For 3D signals, the computational cost is even worse at $O(N^9 \log N)$. This severely limits the adoption of the Wasserstein metric across many domains and in particular for 2D or 3D discrete signals. As a result of this, many authors have developed fast approximations of the Wasserstein metric [Cuturi, 2013, Deshpande et al., 2018, Gerber and Maggioni, 2017, Shirdhonkar and Jacobs, 2008].

We consider the challenge of designing approximations that also serve as strict bounds on the p -Wasserstein metric between discrete measures on a regular grid. In this paper we introduce several efficient algorithms that are based on quantization (or downscaling) of the inputs onto a coarse grid and sum-pooling the measures. We then construct a particular cost matrix for the coarse grid that

takes the original measures into account. This is followed by a correction stage that upscales the solution on the coarse grid to a solution on the original grid and corrects the marginals using iterative proportional-fitting. The upscaling and correction stage is done separately in the primal and dual spaces, to obtain both upper and lower bounds (respectively). Finally, to guarantee the correctness of the bounds without relying on the convergence of the proportional fitting procedure, we introduce an additional total variation correction term.

We developed an efficient GPU implementation of the algorithms described in this paper using the JAX package and tested it on the DOTmark optimal transport benchmark [Schrieber et al., 2017]. We demonstrate that our algorithms achieve significant computational speedups compared to a baseline derived from the entropy-regularized OT. Up to $10\times$ for upper bounds and up to $100\times$ speed up for the lower bounds, while maintaining a low approximation error ($<2\%$) relative to the exact Wasserstein distance.

1.1 Related work

In recent years, the efficient computation of the Wasserstein distance has been a focal point of research, leading to several innovative approaches. The entropy-regularized Sinkhorn algorithm by Cuturi [2013] remains a cornerstone, offering significant computational speedups despite introducing bias. Altschuler et al. [2018] advanced this with near-linear time approximation algorithms. Multiscale methods, as discussed by Gerber and Maggioni [2017] and Mérigot [2011], employ hierarchical strategies to enhance computational efficiency. The benefits of the multiscale approach demonstrated by Feydy et al. [2021] for analyzing brain tractograms by adapting the Sinkhorn algorithm. Other quantization-based methods, notably by Beugnot et al. [2021], improve approximation performance, for sampled continuous measures. For grid data, Solomon et al. [2015] and Chen et al. [2022] exploit structural advantages for speed. In machine learning, Courty et al. [2017] and Alvarez-Melis and Fusi [2020] demonstrate optimal transport’s versatility in domain adaptation. Montesuma et al. [2025] offer a comprehensive survey of recent advances, underscoring the method’s growing impact.

2 Background

Notation We denote the non-negative real numbers by \mathbb{R}_+ and the set of integers $\{1, \dots, n\}$ by $[n]$. The tensor product is denoted by \otimes whereas pointwise multiplication and division are denoted by \odot and \oslash , respectively. The L^p norm of a vector is $\|\cdot\|_p$. The all-ones column vector is $\mathbf{1}_n \in \mathbb{R}^n$. The standard vector inner product is denoted by $\langle \cdot, \cdot \rangle$ and we use the same notation for the inner products of matrices. The support of a matrix $A \in \mathbb{R}^{n \times m}$ is the set of indices of nonzero elements $\text{supp } A = \{(i, j) \in [n] \times [m] \mid A_{i,j} \neq 0\}$. The cardinality of a set S is denoted by $\#S$. δ_x is the Dirac delta function at point x . Complete list of notations used in the paper is provided in Table 7.

2.1 Optimal Transport

In the following, we give a quick review of basic concepts from optimal transport and refer the reader to Peyré and Cuturi [2019] for a more thorough introduction. Consider two discrete probability measures μ, ν with point masses at $\mathcal{X} = \{x_1, \dots, x_n\}$ and $\mathcal{Y} = \{y_1, \dots, y_m\}$ respectively. We can express the measures as a sum of Dirac delta functions,

$$\mu = \sum_{i=1}^n \mu_i \delta_{x_i}, \quad \nu = \sum_{j=1}^m \nu_j \delta_{y_j}. \quad (1)$$

We identify the measures with their non-negative coefficient vectors $\boldsymbol{\mu} \in \mathbb{R}_+^n, \boldsymbol{\nu} \in \mathbb{R}_+^m$. Since μ and ν are probability measures, we must have $\boldsymbol{\mu} \in \Sigma_n$ and $\boldsymbol{\nu} \in \Sigma_m$ where

$$\Sigma_N := \{(p_1, \dots, p_N) \in \mathbb{R}_+^N : p_1 + \dots + p_N = 1\} \quad (2)$$

is the probability simplex. The set of *coupling* matrices between μ and ν is

$$\Pi(\boldsymbol{\mu}, \boldsymbol{\nu}) := \{\pi \in \mathbb{R}_+^{n \times m} \mid \pi \mathbf{1}_m = \boldsymbol{\mu}, \pi^\top \mathbf{1}_n = \boldsymbol{\nu}\}. \quad (3)$$

Each coupling can be viewed as a transport plan between μ and ν where π_{ij} is the amount of mass transported from x_i to y_j . The marginal constraints $\pi \mathbf{1}_m = \boldsymbol{\mu}$ mean that the entire source measure

μ is transported, whereas the constraints $\pi^\top \mathbf{1}_n = \nu$ mean that this transport results in the target measure ν . In particular, the set $\Pi(\mu, \nu)$ always contains the trivial coupling $\pi_\otimes := \mu \otimes \nu$ that distributes every point mass in \mathcal{X} to all point masses in \mathcal{Y} proportionately to ν . Let $C \in \mathbb{R}_+^{n \times m}$ be a ground-cost matrix, where C_{ij} represents the cost of transporting a unit mass from $x_i \in \mathcal{X}$ to $y_j \in \mathcal{Y}$. The Kantorovich problem is the minimization problem that seeks a cost-minimizing coupling between μ and ν ,

$$L_C(\mu, \nu) := \min_{\pi \in \Pi(\mu, \nu)} \langle \pi, C \rangle. \quad (4)$$

This is a linear optimization problem with linear constraints. It admits a dual program,

$$L_C(\mu, \nu) = \max_{(\mathbf{f}, \mathbf{g}) \in \mathcal{R}(C)} \langle \mathbf{f}, \mu \rangle + \langle \mathbf{g}, \nu \rangle, \quad (5)$$

where

$$\mathcal{R}(C) := \{(\mathbf{f}, \mathbf{g}) \in \mathbb{R}^n \times \mathbb{R}^m \mid \forall i, j : f_i + g_j \leq C_{ij}\} \quad (6)$$

is the set of admissible dual potentials, also known as Kantorovich potentials. Given a distance metric $\rho : \mathcal{X} \times \mathcal{X} \rightarrow \mathbb{R}_+$, for any $p \geq 1$ the *Wasserstein- p* metric is a metric over the space of discrete probability measures with point masses at $\mathcal{X} = \{x_1, \dots, x_n\}$, defined as $\mathcal{W}_p(\mu, \nu) := L_C(\mu, \nu)^{\frac{1}{p}}$ where $C_{ij} = \rho(x_i, y_j)^p$.

2.2 Measure coarsening

Consider a d -dimensional regular grid $\mathcal{X} = [N]^d$. Suppose that N is a multiple of some scale factor $\kappa \in \mathbb{N}$. In that case we may subdivide the grid along the axes into a set $\mathbb{X} = \{X_1, \dots, X_{n^d}\}$ of non-overlapping hypercubes of cardinality κ^d that cover the entire grid \mathcal{X} . We define the coarse grid $\tilde{\mathcal{X}} := \{\tilde{x}_1, \dots, \tilde{x}_{n^d}\}$ as the set of all hypercube centers, with $\tilde{x}_k = \text{mean}(X_k)$. Given a discrete measure $\mu \in \Sigma_{N^d}$ over the grid \mathcal{X} , we define a coarsened discrete measure by placing the mass associated with each hypercube at its center point, $\tilde{\mu} = \sum_{k=1}^{n^d} \mu(X_k) \delta_{\tilde{x}_k}$. The coarsening of the regular grid corresponds to the `SumPool` and `AvgPool` operations on the measure and the coordinates, respectively, with size and stride κ .

3 Methods

In this section, we describe several algorithms for computing bounds of the Wasserstein distance $\mathcal{W}_p(\mu, \nu)$ on a regular grid.

3.1 Bounds based on Entropy regularized OT

Entropy regularized optimal transport, also known as Sinkhorn distance [Cuturi, 2013], adds an entropy term \mathcal{H} to the primal:

$$L_C^\varepsilon(\mu, \nu) := \min_{\pi \in \Pi(\mu, \nu)} \langle \pi, C \rangle - \varepsilon \mathcal{H}(\pi). \quad (7)$$

This makes the problem strongly convex and solvable using Sinkhorn iterations [Knopp and Sinkhorn, 1967]. In this section we will show how computing entropy regularized OT can be used to construct upper and lower bounds on the exact Wasserstein distance.

Lower bound The dual form of the Sinkhorn distance is

$$L_C^\varepsilon(\mu, \nu) := \max_{\mathbf{f} \in \mathbb{R}^n, \mathbf{g} \in \mathbb{R}^m} \langle \mathbf{f}, \mu \rangle + \langle \mathbf{g}, \nu \rangle - \varepsilon \langle e^{\mathbf{f}/\varepsilon}, K e^{\mathbf{g}/\varepsilon} \rangle \quad (8)$$

where $K_{ij} := e^{-C_{ij}/\varepsilon}$ is the Gibbs kernel. The algorithmic solution, defined by the use of a finite number of iterations t that achieves some stopping criteria, is known to satisfy a lower bound. Summarized in the following proposition.

Proposition 3.1. *Let $\hat{\mathbf{f}}_\varepsilon^{(t)}, \hat{\mathbf{g}}_\varepsilon^{(t)}$ be the iterations of the Sinkhorn distance algorithm in step $t \in \mathbb{N}$.*

$$\langle \hat{\mathbf{f}}_\varepsilon^{(t)}, \mu \rangle + \langle \hat{\mathbf{g}}_\varepsilon^{(t)}, \nu \rangle \leq L_C(\mu, \nu) \quad (9)$$

as soon as $t \geq 1$.

This follows directly from Peyré and Cuturi [2019, Propositions 4.5, 4.8], so we can define $\underline{\mathcal{W}}_{p,\varepsilon}(\mu, \nu) := (\langle \hat{\mathbf{f}}_\varepsilon^{(t)}, \mu \rangle + \langle \hat{\mathbf{g}}_\varepsilon^{(t)}, \nu \rangle)^{\frac{1}{p}} \leq \mathcal{W}_p(\mu, \nu)$ for all $p \geq 1$.

Upper bound Consider d -dimensional regular grids with side length $N \in \mathbb{N}$, $\mathcal{X} = \mathcal{Y} = [N]^d$, with discrete measures $\mu, \nu \in \Sigma_{N^d}$. Although the converged regularized optimal coupling

$$\pi_\varepsilon^* = \arg \min_{\pi \in \Pi(\mu, \nu)} \langle \pi, C \rangle - \varepsilon \mathcal{H}(\pi) \quad (10)$$

defines an upper bound on the optimal transport $\langle \pi_\varepsilon^*, C \rangle \geq L_C(\mu, \nu)$, the algorithmic solution $\hat{\pi}_\varepsilon^{(t)}$ does not. Since the marginals $\hat{\mu}_\varepsilon^{(t)} = \hat{\pi}_\varepsilon^{(t)} \mathbf{1}_N$, $\hat{\nu}_\varepsilon^{(t)} = (\hat{\pi}_\varepsilon^{(t)})^\top \mathbf{1}_N$ do not identify with the couplings μ, ν . We bound the effect of this difference using the weighted total variation. For some $x_0 \in \mathcal{X}$, using distance weights $\mathbf{w} = \{\rho(x_0, x)^p\}_{x \in \mathcal{X}}$ the Wasserstein- p distance is controlled by *weighted* total variation [Villani, 2009],

$$\mathcal{TV}_p^{\mathbf{w}}(\mu, \nu) := 2^{1-\frac{1}{p}} \langle \mathbf{w}, |\mu - \nu| \rangle^{\frac{1}{p}} \geq \mathcal{W}_p(\mu, \nu). \quad (11)$$

Here $|\cdot|$ is the element-wise absolute value.

Defining the total variation corrected regularization-based upper bound

$$\bar{\mathcal{W}}_{p,\varepsilon}(\mu, \nu) := \langle \hat{\pi}_\varepsilon^{(t)}, C \rangle^{\frac{1}{p}} + \Delta_{\hat{\mu}_\varepsilon^{(t)}} + \Delta_{\hat{\nu}_\varepsilon^{(t)}}, \quad (12)$$

where $\Delta_{\hat{\mu}_\varepsilon^{(t)}} = \mathcal{TV}_p^{\mathbf{w}}(\hat{\mu}_\varepsilon^{(t)}, \mu)$, $\Delta_{\hat{\nu}_\varepsilon^{(t)}} = \mathcal{TV}_p^{\mathbf{w}}(\nu, \hat{\nu}_\varepsilon^{(t)})$ are the marginal corrections with weights $\mathbf{w} = \{\rho(\bar{x}, x_i)\}_i$ are taken from the center of the measure $\bar{x} = \text{mean}(\mathcal{X})$. Using the triangle inequality for the Wasserstein metric, we can write

Lemma 3.2. *Let $\mu, \hat{\mu}, \nu, \hat{\nu} \in \Sigma_{N^d}$ discrete measures on $\mathcal{X} = [N]^d$, and $\hat{\pi} \in \Pi(\hat{\mu}, \hat{\nu})$ is a coupling between $\hat{\mu}$ and $\hat{\nu}$. For $p \geq 1$,*

$$\mathcal{W}_p(\mu, \nu) \leq \langle \hat{\pi}, C \rangle^{\frac{1}{p}} + \Delta_{\hat{\mu}} + \Delta_{\hat{\nu}} \quad (13)$$

Combining this with (12) shows that $\mathcal{W}_p(\mu, \nu) \leq \bar{\mathcal{W}}_{p,\varepsilon}(\mu, \nu)$.

Proposition 3.3. *Let $\mu, \hat{\mu}, \nu, \hat{\nu} \in \Sigma_n$ be discrete measures in \mathcal{X} and $\xi > 0$, satisfying the convergence criteria $\|\hat{\mu} - \mu\|_1 + \|\nu - \hat{\nu}\|_1 < \xi$. The sum of the marginal corrections is bounded,*

$$\Delta_{\hat{\mu}} + \Delta_{\hat{\nu}} < 2^{2-\frac{2}{p}} \xi^{\frac{1}{p}} r \quad (14)$$

where $r := \max_{x \in \mathcal{X}} \{\rho(\bar{x}, x)\}$ is radius of \mathcal{X} .

Proofs for Lemma 3.2 and Proposition 3.3 are provided in Appendix C.1.

3.2 Weighted-cost upper bound

In this subsection we consider an approach to bound Wasserstein distance by down-scaling the grid \mathcal{X} to $\tilde{\mathcal{X}} = \tilde{\mathcal{Y}}$ and the measures to $\tilde{\mu}, \tilde{\nu} \in \Sigma_{n^d}$ using regular hypercubes as described in Section 2.2. We define the marginally weighted coarse cost

$$\bar{C}_{k\ell} := \frac{1}{\mu(X_k)\nu(Y_\ell)} \sum_{x \in X_k, y \in Y_\ell} \rho(x, y)^p \mu(x)\nu(y). \quad (15)$$

It follows that $\bar{C} = \text{SumPool}(C \odot \pi_\otimes, \kappa) \odot \text{SumPool}(\pi_\otimes, \kappa)$, which can be used efficiently for small enough grids. Then we compute the optimal coupling for the marginally weighted coarse cost using network simplex solver [Bonnel et al., 2011], defining an upper bound

$$\bar{\mathcal{W}}_p^\otimes := L_{\bar{C}}(\tilde{\mu}, \tilde{\nu})^{\frac{1}{p}}. \quad (16)$$

Theorem 3.4. *The optimal transport loss under the marginally weighted coarse cost $L_{\bar{C}}(\tilde{\mu}, \tilde{\nu})$ is an upper bound to the optimal transport loss $L_C(\mu, \nu)$, and similarly for the Wasserstein distance,*

$$L_{\bar{C}}(\tilde{\mu}, \tilde{\nu})^{\frac{1}{p}} \geq \mathcal{W}_p(\mu, \nu). \quad (17)$$

The proof uses an auxiliary coupling transferring the mass between each pair of sub-regions (X_i, Y_j) using the trivial coupling, weighted by a coarse coupling, choosing the optimal coarse coupling. A detailed proof is provided in Appendix C.2.

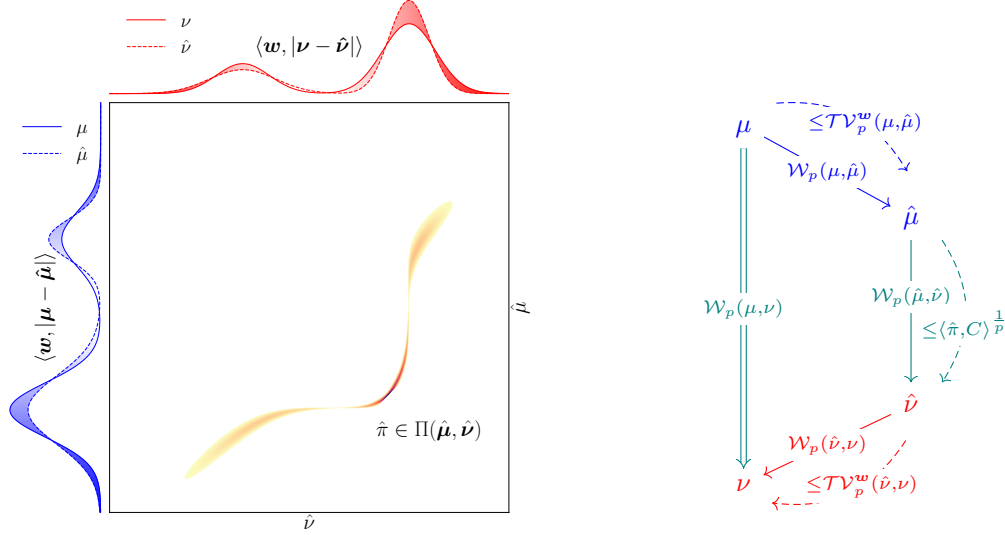


Figure 1: Optimal transport bounds visualization. Left: Illustration of optimal transport between discrete probability measures. Right: Diagram showing the relationship between measures and their Wasserstein distances.

3.3 Min-cost lower bound

For the same coarsening, we define the locally minimal cost $C_{k\ell}^{\min} := \min_{x \in X_k, y \in Y_\ell} \rho(x, y)^p$, and compute the optimal coupling for this coarse cost using a network simplex solver, yielding a lower bound $\underline{\mathcal{W}}_p^{\min} := L_{C^{\min}}(\tilde{\mu}, \tilde{\nu})^{\frac{1}{p}}$. The following theorem is proved in Appendix C.3.

Theorem 3.5. *The coarse optimal transport cost set by the locally minimal cost, is a lower bound of the optimal transport. $L_{C^{\min}}(\tilde{\mu}, \tilde{\nu}) \leq L_C(\mu, \nu)$.*

3.4 Primal upscaling upper bound

In this approach we upscale an optimal coupling for the coarse cost $\tilde{c}_{k\ell} = \rho(\tilde{x}_k, \tilde{y}_\ell)^p$ computed using a network simplex solver $\tilde{\pi}^* = \arg \min_{\tilde{\pi} \in \Pi(\tilde{\mu}, \tilde{\nu})} \langle \tilde{\pi}, \tilde{C} \rangle$ back to the original problem size.

Up-scaled coupling A coupling matrix π of dimensions $n^d \times n^d$ can equivalently be represented as a $2d$ -tensor of the shape $n \times n \times \dots \times n$. We formally define operations for reshaping matrices into tensors and back. Let reshape be a cardinality-preserving transformation from \mathbf{A} to \mathbf{B} such that $a_{ij} = b_{u_1, \dots, u_d, v_1, \dots, v_d}$ where (u_1, \dots, u_d) is a multi-index that corresponds to a matrix row by $i = 1 + \sum_{k=1}^d u_k n^{k-1}$. Similarly the multi-index (v_1, \dots, v_d) corresponds to the column index j . Reshaping the coarse optimal coupling $\tilde{\pi}^*$ into a $2d$ -tensor $\tilde{\mathbf{P}}^*$, we up-scale the optimal coupling using a normalized positive-valued kernel \mathbf{K} , a $2d$ -tensor representing a hypercube of width κ .

$$\hat{\mathbf{P}} := \tilde{\mathbf{P}}^* \otimes \mathbf{K}. \quad (18)$$

By inversely reshaping the up-scaled tensor $\hat{\mathbf{P}}$ into an up-scaled matrix $\hat{\pi}$, we obtain the approximate up-scaled coupling. Using a uniform kernel \mathbf{K} is equivalent to nearest-neighbor interpolation.

Lemma 3.6. *Using a normalized positive-valued kernel \mathbf{K} ensures $\hat{\pi}$ represents a coupling. Satisfying $\hat{\pi} \in \mathbb{R}_+^{N^d \times N^d}$ and $\sum_{i=1}^{N^d} \sum_{j=1}^{N^d} \hat{\pi}_{ij} = 1$, such that $\hat{\pi} \in \Pi(\hat{\pi} \mathbf{1}_{N^d}, \hat{\pi}^\top \mathbf{1}_{N^d})$.*

Iterative proportional fitting The approximate up-scaled coupling is ξ -fitted into $\hat{\pi}_\xi = \text{diag}(\mathbf{a}) \hat{\pi} \text{diag}(\mathbf{b})$ by iterative proportional fitting using Sinkhorn's theorem, until the marginals $\hat{\mu}_\xi = \mathbf{a} \odot (\hat{\pi} \mathbf{b})$, $\hat{\nu}_\xi = \mathbf{b} \odot (\hat{\pi}^\top \mathbf{a})$ are converged to $\|\hat{\mu}_\xi - \mu\|_1 + \|\nu - \hat{\nu}_\xi\|_1 < \xi$, where $\mathbf{a}, \mathbf{b} \in \mathbb{R}_+^{N^d}$ are the vector scale factors, yielding the approximation $\widehat{\mathcal{W}}_p(\mu, \nu) := \langle \hat{\pi}_\xi, C \rangle^{\frac{1}{p}}$.

Upper bound Using weighted total variation (Equation (11)) we define an upscaling upper bound

$$\overline{\mathcal{W}}_p(\mu, \nu) := \widehat{\mathcal{W}}_p(\mu, \nu) + \Delta_{\hat{\mu}_\xi} + \Delta_{\hat{\nu}_\xi}, \quad (19)$$

Theorem 3.7 (Upscaling Upper Bound). $\overline{\mathcal{W}}_p(\mu, \nu)$ is upper bound of the Wasserstein distance,

$$\mathcal{W}_p(\mu, \nu) \leq \overline{\mathcal{W}}_p(\mu, \nu). \quad (20)$$

Proof of Theorem 3.7. The up-scaled matrix $\hat{\pi} \in \Pi(\hat{\pi} \mathbf{1}_{N^d}, \hat{\pi}^\top \mathbf{1}_{N^d})$ is normalized as a coupling, by Lemma 3.6, and $\hat{\pi}_\xi$ retains this normalization, by Sinkhorn's theorem. $\overline{\mathcal{W}}_p(\mu, \nu)$ is than an upper bound of the Wasserstein distance, by Lemma 3.2. \square

Remark 3.8. Considering $\mathcal{X} = [N]^d$ with L^2 norm, the radius becomes $r = \frac{1}{2}d^{\frac{1}{2}}N$ (see Proposition 3.3) such that the weighted total variation correction $\Delta_{\hat{\mu}} + \Delta_{\hat{\nu}}$ is at most $2^{1-\frac{2}{p}}d^{\frac{1}{2}}N\xi^{\frac{1}{p}}$. Negligible for $\xi \ll N^{-p}$, and can be ignored for many practical use cases.

3.5 Dual upscaling lower bound

We construct a lower bound for the Wasserstein distance $\mathcal{W}_p(\mu, \nu)$ by solving a down-scaled optimal transport problem using coarsened measures. The coarse optimal Kantorovich potentials are than up-scaled using a multi-linear interpolation and improved using a c-transform. Considering the same setting as in Section 3.4, we solve for the optimal potentials of the down-scaled discrete measures

$$(\tilde{\mathbf{f}}^*, \tilde{\mathbf{g}}^*) = \arg \max_{(\tilde{\mathbf{f}}, \tilde{\mathbf{g}}) \in \mathcal{R}(\tilde{C})} \langle \tilde{\mathbf{f}}, \tilde{\boldsymbol{\mu}} \rangle + \langle \tilde{\mathbf{g}}, \tilde{\boldsymbol{\nu}} \rangle \quad (21)$$

and evaluate the dual transport cost at the original scale by up-scaling the optimal potentials. Up-scaling can be performed by any multivariate interpolation method such as nearest-neighbor, spline, multi-linear and polynomial methods. Using an interpolation function $R : \mathcal{X} \cup \tilde{\mathcal{X}} \rightarrow \mathbb{R}$, the up-scaled potential $\hat{\mathbf{f}}$ is defined by

$$\hat{\mathbf{f}} := \{R_{\tilde{\mathbf{f}}, \tilde{\mathcal{X}}}(x_i)\}_{i \in [N^d]}. \quad (22)$$

An important property of the dual formulation is that for every potential $\mathbf{f} \in \mathbb{R}^n$ we can easily find a *tight* potential $\mathbf{f}^c \in \mathbb{R}^m$ such that $(\mathbf{f}, \mathbf{f}^c) \in \mathcal{R}(C)$, by $f_j^c := \min_i C_{ij} - f_i$. This is known as a *c-transform*. It can be shown that repeating this process once more achieves a tight pair $(\mathbf{f}^c, \mathbf{f}^{cc}) \in \mathcal{R}(C)$, where $f_i^{cc} := \min_j C_{ij} - f_j^c$. Thus, a lower bound is guaranteed by using the c-transform to generate the potential pair from the up-scaled potential $\mathbf{f} = \hat{\mathbf{f}}^{cc}$ and $\mathbf{g} = \hat{\mathbf{f}}^c$, which yields the upscaling lower bound

$$\underline{\mathcal{W}}_p(\mu, \nu) := (\langle \hat{\mathbf{f}}, \boldsymbol{\mu} \rangle + \langle \hat{\mathbf{g}}, \boldsymbol{\nu} \rangle)^{\frac{1}{p}}. \quad (23)$$

Since by the admissibility of a c-transformed pair $(\mathbf{f}, \mathbf{g}) \in \mathcal{R}(C)$, we can write

Proposition 3.9. *Considering an approximate potential $\hat{\mathbf{f}} \in \mathbb{R}^{N^d}$. For $\mathbf{f} = \hat{\mathbf{f}}^{cc}$ and $\mathbf{g} = \hat{\mathbf{f}}^c$*

$$\langle \mathbf{f}, \boldsymbol{\mu} \rangle + \langle \mathbf{g}, \boldsymbol{\nu} \rangle \leq L_C(\mu, \nu). \quad (24)$$

4 Computational complexity analysis

The quantization-based bounds involve the following steps: computing the Wasserstein metric on the quantized measures, upscaling the dual potentials or couplings to the original scale, and the calculation of weighted total variation correction terms. The latter is calculated in linear time and space, thus negligible w.r.t. the other steps. In the following, we detail the computational gains provided by the proposed methods.

Downscaled optimal transport The solution to the Kantorovich problem of the scaled measures can be solved by dedicated linear programming methods, such as the network simplex used in Bonneel et al. [2011], with $O(n^{3d} \log n)$ time complexity [Ahuja et al., 1993]. By solving only for the optimal transport of the coarse measures, we produce a computational speedup of $\Theta(\kappa^{3d})$ (up to log factors). The space complexity can also be significantly reduced, since one can avoid storing the full cost matrix of size $N^d \times N^d$, by using coarse cost matrices, e.g. \bar{C} , C^{\min} , and \tilde{C} of size $n^d \times n^d$, realizing a memory gain of $\Theta(\kappa^{2d})$.

Upscaled optimal coupling The optimal coarse coupling $\tilde{\pi}^*$ is a sparse matrix with at most $2n^d - 1$ positive entries [Peyré and Cuturi, 2019, Proposition 3.4]. Thus, the up-scaled approximate coupling from Equation (18) conserves this sparsity with $\#\text{supp } \hat{\pi} \leq \kappa^{2d}(2n^d - 1)$, allowing to calculate the approximate optimal transport

$$\langle \hat{\pi}_\xi, C \rangle = \sum_{(i,j) \in \text{supp } \hat{\pi}} \overbrace{a_i \hat{\pi}_{ij} b_j}^{(\hat{\pi}_\xi)_{ij}} \rho(x_i, y_j)^p. \quad (25)$$

without impacting the total time and space complexity of the coarse optimal transport solution.

$$\frac{\#C}{\#\text{supp } \hat{\pi}} = \frac{N^{2d}}{\kappa^{2d}(2n^d - 1)} = \Theta((N/\kappa)^d). \quad (26)$$

Lazy c-transform To reduce the memory requirements of Equation (23), we evaluate the c-transform on-demand (i.e. "lazy") without storing the entire cost matrix C .

$$g_j \leftarrow \min_i \rho(x_i, y_j)^p - \hat{f}_i \quad (27)$$

$$f_i \leftarrow \min_j \rho(x_i, y_j)^p - g_j \quad (28)$$

Method	Time Complexity	Space Complexity
Entropic Regularization-Based Bounds [Lin et al., 2022]	$\tilde{O}((n\kappa)^{2d}/\varepsilon^2)$	$O((n\kappa)^{2d})$
Quantization-Based Bounds	$\tilde{O}(n^{3d})$	$O(n^{2d})$

Table 1: Complexity of different bounds in terms of the fine-scale cardinality $\#\mathcal{X} = N^d = (n\kappa)^d$. The first row corresponds to the methods in Section 3.1 and the second to Sections 3.2 to 3.5.

5 Experiments

The algorithms were implemented in Python and optimized for GPU acceleration using JAX numerical computation library [Bradbury et al., 2018]. For entropy regularized optimal transport we used OTT-JAX [Cuturi et al., 2022] and POT [Flamary et al., 2021] for exact optimal transport. The methods were benchmarked on a machine using an NVIDIA L40 GPU and AMD EPYC 9654 CPU.

DOTmark The methods were evaluated on 2D images from the discrete optimal transport benchmark [Schrieber et al., 2017], using $\rho = L^2$ the euclidean metric, at $p = \{1, 2\}$. To examine the effect of the scaling factor, the quantization-based methods were evaluated using $\kappa = \{2, 4\}$. To examine the effect of the entropic-regularization parameter, the regularization-based methods were evaluated using $\varepsilon = \{0.001N^p, 0.004N^p\}$ explicitly dependent on N^p term to avoid large $\|C\|_\infty/\varepsilon$ causing numerical instability [Altschuler et al., 2018], since $\|C\|_\infty \propto N^p$ in our setting. For upper bounds, while at $p = 1$ the entropic-regularization upper bound at $\varepsilon = 0.001N^p$ delivers the best approximation, summarized in Table 2, it does so with significant impact on the computation time, as seen in Figure 2. Otherwise, both for upper and lower bound the quantization methods produce the best approximations at $\kappa = 2$, while computing with relative time second only to the quantization methods scaled at $\kappa = 4$.

EMDB In the field of structural biology, approximations of the Wasserstein metric are increasingly being used on 2D projection images and 3D volumetric reconstructions of proteins and other macromolecules. Specific applications include molecular alignment, clustering and dimensionality reduction, with most methods substituting the Wasserstein metric with a crude approximation that is fast to compute [Rao et al., 2020, Riahi et al., 2023, Singer and Yang, 2024, Kileel et al., 2021]. We evaluate our algorithms in a challenging 3D alignment setting, where we wish to compute the Wasserstein- p metric $p \in \{1, 2\}$ between rotated 3D density maps of the same molecule. The volumetric density maps are downloaded from the Electron Microscopy Data Bank (EMDB) [wwPDB Consortium, 2024] using the ASPIRE package [Wright et al., 2025]. Figure 4 shows the computed

		Upper Bounds						Lower Bounds					
		Weighted-Cost		Primal Upscaling		Entropic Regularization		Dual Upscaling		Min-Cost		Entropic Regularization	
Class	p	κ_2	κ_4	κ_2	κ_4	ε_1	ε_4	κ_2	κ_4	κ_2	κ_4	ε_1	ε_4
Classic Images	1	3.1%	11.0%	9.6%	23.0%	0.9%	5.2%	0.3%	0.7%	10.0%	27.0%	24.0%	88.0%
		$\pm 2.0%$	$\pm 7.1%$	$\pm 4.1%$	$\pm 9.9%$	$\pm 0.5%$	$\pm 2.1%$	$\pm 0.2%$	$\pm 0.4%$	$\pm 6.4%$	$\pm 16.0%$	$\pm 8.3%$	$\pm 15.0%$
	2	1.6%	7.9%	2.2%	8.8%	14.0%	44.0%	0.7%	2.4%	13.0%	33.0%	98.0%	100.0%
		$\pm 1.2%$	$\pm 5.2%$	$\pm 1.4%$	$\pm 5.5%$	$\pm 8.8%$	$\pm 25.0%$	$\pm 0.5%$	$\pm 1.6%$	$\pm 3.7%$	$\pm 8.8%$	$\pm 8.4%$	$\pm 0.0%$
Microscopy	1	0.9%	3.4%	2.4%	6.5%	0.4%	2.0%	0.4%	0.9%	6.2%	17.0%	9.6%	38.0%
		$\pm 1.7%$	$\pm 5.9%$	$\pm 3.2%$	$\pm 8.4%$	$\pm 0.3%$	$\pm 2.0%$	$\pm 0.5%$	$\pm 0.9%$	$\pm 4.2%$	$\pm 10.0%$	$\pm 7.1%$	$\pm 22.0%$
	2	0.5%	2.2%	0.7%	2.7%	3.8%	11.0%	0.2%	0.7%	5.5%	16.0%	30.0%	90.0%
		$\pm 0.7%$	$\pm 3.5%$	$\pm 1.0%$	$\pm 3.9%$	$\pm 5.9%$	$\pm 18.0%$	$\pm 0.4%$	$\pm 1.2%$	$\pm 3.4%$	$\pm 8.4%$	$\pm 32.0%$	$\pm 19.0%$
Shapes	1	1.1%	3.6%	3.2%	7.8%	0.7%	2.6%	0.5%	1.0%	7.3%	20.0%	13.0%	51.0%
		$\pm 2.2%$	$\pm 4.8%$	$\pm 2.6%$	$\pm 6.3%$	$\pm 2.5%$	$\pm 2.2%$	$\pm 2.8%$	$\pm 3.0%$	$\pm 5.2%$	$\pm 11.0%$	$\pm 8.1%$	$\pm 22.0%$
	2	1.2%	3.2%	1.4%	3.6%	5.1%	15.0%	0.9%	1.7%	7.7%	20.0%	52.0%	99.0%
		$\pm 4.5%$	$\pm 5.0%$	$\pm 4.5%$	$\pm 5.0%$	$\pm 6.2%$	$\pm 17.0%$	$\pm 5.1%$	$\pm 5.6%$	$\pm 6.1%$	$\pm 9.2%$	$\pm 34.0%$	$\pm 9.6%$

Table 2: Accuracy comparison of different methods showing the mean \pm standard deviation of the relative error computed across all the pairwise distances in the DOTmark class at 128×128 resolution. Each method is evaluated at different fidelity level $\kappa_2 = 2$ and $\kappa_4 = 4$ and different values of $\varepsilon_1 = 1 \cdot 10^{-3}N^p$ and $\varepsilon_4 = 4 \cdot 10^{-3}N^p$.

bounds for rotations between 0° and 180° of the Plasmodium falciparum 80S ribosome 3D density map [Wong et al., 2014].

Plots for other molecules are shown in the supplementary material. Dual upscaling (lower bound) and weighted-cost (upper bound) methods at $\kappa = 2$ provide the best approximations. A summary of the computational speed-up is provided in Table 3.

		Upper Bounds						Lower Bounds					
		Weighted-Cost		Primal Upscaling		Entropic Regularization		Dual Upscaling		Min-Cost		Entropic Regularization	
p		κ_2	κ_4	κ_2	κ_4	ε_1	ε_4	κ_2	κ_4	κ_2	κ_4	ε_1	ε_4
1		0.22%	0.12%	1.09%	27.23%	130.95%	144.97%	0.55%	0.33%	0.20%	0.11%	190.88%	197.35%
		$\pm 0.06%$	$\pm 0.26%$	$\pm 0.34%$	$\pm 15.99%$	$\pm 29.46%$	$\pm 39.00%$	$\pm 0.21%$	$\pm 0.21%$	$\pm 0.06%$	$\pm 0.29%$	$\pm 58.51%$	$\pm 52.12%$
2		0.22%	0.06%	0.30%	0.16%	164.64%	171.42%	0.19%	0.04%	0.21%	0.04%	195.49%	197.76%
		$\pm 0.04%$	$\pm 0.02%$	$\pm 0.07%$	$\pm 0.08%$	$\pm 42.18%$	$\pm 41.89%$	$\pm 0.05%$	$\pm 0.02%$	$\pm 0.05%$	$\pm 0.02%$	$\pm 42.43%$	$\pm 44.34%$

Table 3: Computation time relative to the exact Wasserstein distance computation for 3D Cryo-EM data at $32 \times 32 \times 32$ resolution. Results show mean \pm standard deviation across rotations.

6 Conclusion and discussion

In this paper, we proposed several methods for computing fast approximations that lower or upper-bound the Wasserstein metric between discrete distributions on a regular grid. Our methods are based on the solution of lower-resolution OT problems that are then upsampled and corrected to yield upper and lower bounds to the original problem. Our experiments on 2D images and 3D volumetric data demonstrate significant improvements in computational efficiency and accuracy compared to bounds based on entropic OT. Despite the considerable computational speedups resulting from our methods compared to the only apparent alternative for exact Wasserstein bounds, the methods are still much slower compared to many almost linear time state-of-the-art approximation methods practitioners use in practice for such datasets. Looking forward, our approach could be refined and extended by exploring different interpolation methods for the upscaling stage and multi-scale approaches. Finally, despite the paper’s focus, the methods could also be extended to domains beyond regular grids such as point clouds in \mathbb{R}^n and graphs.

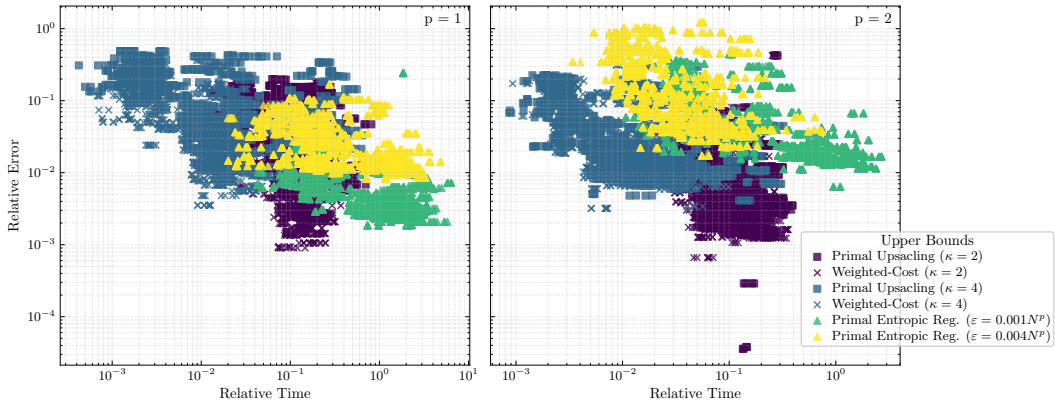


Figure 2: Efficiency of Wasserstein Upper Bounds

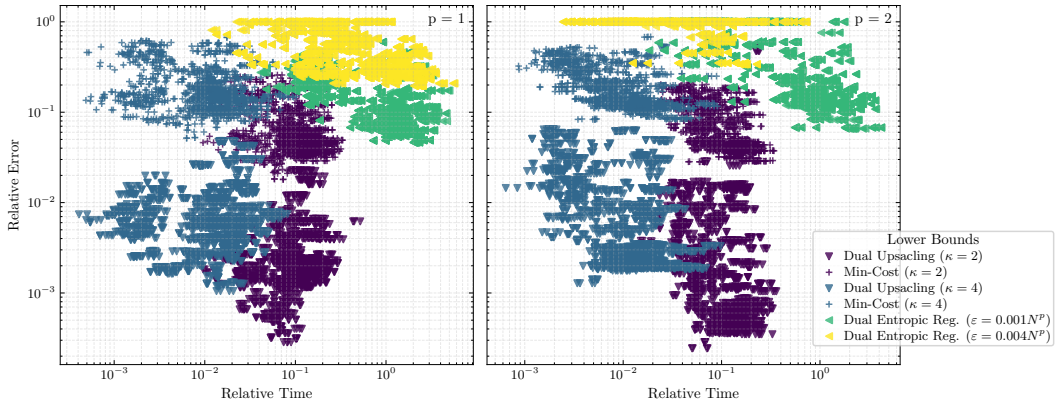


Figure 3: Efficiency of Wasserstein Lower Bounds

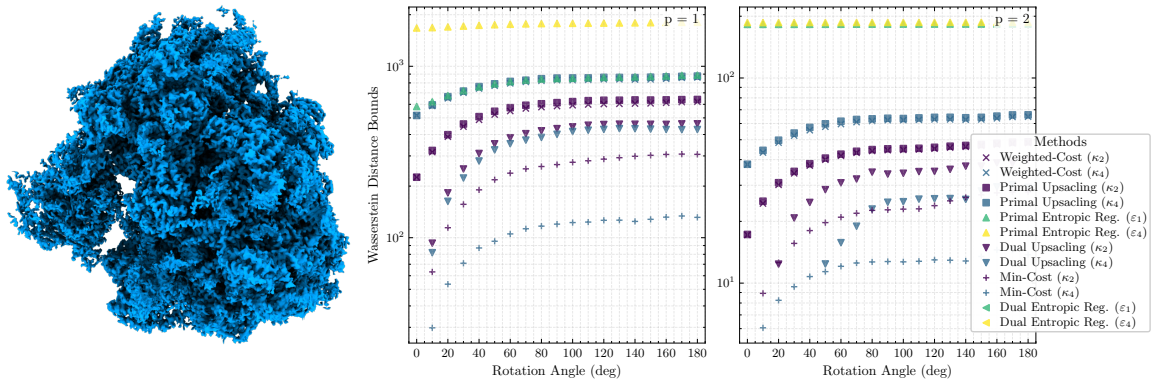


Figure 4: Wasserstein distance bounds between rotated 3D density maps of the 80S ribosome. The left panel shows an isosurface plot of the 3D density map that we rotated around the z -axis. The other two panels compare the different algorithms for producing upper and lower bounds on the Wasserstein- p metric. (center) $p = 1$; (right) $p = 2$.

References

- R. K. Ahuja, T. L. Magnanti, and J. B. Orlin. *Network Flows: Theory, Algorithms, and Applications*. Prentice-Hall, Inc., USA, Feb. 1993. ISBN 978-0-13-617549-0.
- J. Altschuler, J. Weed, and P. Rigollet. Near-linear time approximation algorithms for optimal transport via Sinkhorn iteration, Feb. 2018.
- D. Alvarez-Melis and N. Fusi. Geometric Dataset Distances via Optimal Transport. In *Advances in Neural Information Processing Systems*, volume 33, pages 21428–21439. Curran Associates, Inc., 2020. URL <https://proceedings.neurips.cc/paper/2020/hash/f52a7b2610fb4d3f74b4106fb80b233d-Abstract.html>.
- M. Arjovsky, S. Chintala, and L. Bottou. Wasserstein Generative Adversarial Networks. In *Proceedings of the 34th International Conference on Machine Learning*, pages 214–223. PMLR, July 2017. URL <https://proceedings.mlr.press/v70/arjovsky17a.html>.
- A. Bartesaghi, A. Merk, M. J. Borgnia, J. L. S. Milne, and S. Subramaniam. Prefusion structure of trimeric HIV-1 envelope glycoprotein determined by cryo-electron microscopy. *Nature Structural & Molecular Biology*, 20(12):1352–1357, Dec. 2013. ISSN 1545-9985. doi:10.1038/nsmb.2711.
- G. Beugnot, A. Genevay, K. Greenewald, and J. Solomon. Improving approximate optimal transport distances using quantization. In *Proceedings of the Thirty-Seventh Conference on Uncertainty in Artificial Intelligence*, pages 290–300. PMLR, Dec. 2021. URL <https://proceedings.mlr.press/v161/beugnot21a.html>.
- N. Bonneel, M. van de Panne, S. Paris, and W. Heidrich. Displacement interpolation using Lagrangian mass transport. *ACM Transactions on Graphics*, 30(6):1–12, Dec. 2011. ISSN 0730-0301. doi:10.1145/2070781.2024192.
- J. Bradbury, R. Frostig, P. Hawkins, M. J. Johnson, C. Leary, D. Maclaurin, G. Necula, A. Paszke, J. VanderPlas, S. Wanderman-Milne, and Q. Zhang. JAX: Composable transformations of Python+NumPy programs, 2018. URL <http://github.com/jax-ml/jax>.
- Y. Chen, C. Li, and Z. Lu. Computing Wasserstein- p Distance Between Images with Linear Cost. In *2022 IEEE/CVF Conference on Computer Vision and Pattern Recognition (CVPR)*, pages 509–518, New Orleans, LA, USA, June 2022. IEEE. ISBN 978-1-66546-946-3. doi:10.1109/CVPR52688.2022.00060.
- N. Courty, R. Flamary, D. Tuia, and A. Rakotomamonjy. Optimal Transport for Domain Adaptation. *IEEE Transactions on Pattern Analysis and Machine Intelligence*, 39(9):1853–1865, Sept. 2017. ISSN 1939-3539. doi:10.1109/TPAMI.2016.2615921.
- M. Cuturi. Sinkhorn Distances: Lightspeed Computation of Optimal Transport. In *Advances in Neural Information Processing Systems*, volume 26. Curran Associates, Inc., 2013.
- M. Cuturi, L. Meng-Papaxanthos, Y. Tian, C. Bunne, G. Davis, and O. Teboul. Optimal Transport Tools (OTT): A JAX Toolbox for all things Wasserstein, Jan. 2022.
- I. Deshpande, Z. Zhang, and A. G. Schwing. Generative Modeling Using the Sliced Wasserstein Distance. In *Proceedings of the IEEE Conference on Computer Vision and Pattern Recognition*, pages 3483–3491, 2018. URL https://openaccess.thecvf.com/content_cvpr_2018/html/Deshpande_Generative_Modeling_Using_CVPR_2018_paper.html.
- J. Feydy, P. Roussillon, A. Trounev, and P. Gori. Fast and Scalable Optimal Transport for Brain Tractograms, July 2021.
- R. Flamary, N. Courty, A. Gramfort, M. Z. Alaya, A. Boisbunon, S. Chambon, L. Chapel, A. Corenflos, K. Fatras, N. Fournier, L. Gautheron, N. T. H. Gayraud, H. Janati, A. Rakotomamonjy, I. Redko, A. Rolet, A. Schutz, V. Seguy, D. J. Sutherland, R. Tavenard, A. Tong, and T. Vayer. POT: Python Optimal Transport. *Journal of Machine Learning Research*, 22(78):1–8, 2021. ISSN 1533-7928. URL <http://jmlr.org/papers/v22/20-451.html>.

- S. Gerber and M. Maggioni. Multiscale strategies for computing optimal transport. *The Journal of Machine Learning Research*, 18(1):2440–2471, Jan. 2017. ISSN 1532-4435.
- J. Kileel, A. Moscovich, N. Zelesko, and A. Singer. Manifold Learning with Arbitrary Norms. *Journal of Fourier Analysis and Applications*, 27(5), Oct. 2021. ISSN 1069-5869, 1531-5851. doi:[10.1007/s00041-021-09879-2](https://doi.org/10.1007/s00041-021-09879-2).
- P. Knopp and R. Sinkhorn. Concerning nonnegative matrices and doubly stochastic matrices. *Pacific Journal of Mathematics*, 21(2):343–348, Jan. 1967. ISSN 0030-8730. URL <https://projecteuclid.org/journals/pacific-journal-of-mathematics/volume-21/issue-2/Concerning-nonnegative-matrices-and-doubly-stochastic-matrices/pjm/1102992505.full>.
- M. Kusner, Y. Sun, N. Kolkin, and K. Weinberger. From Word Embeddings To Document Distances. In *Proceedings of the 32nd International Conference on Machine Learning*, pages 957–966. PMLR, June 2015. URL <https://proceedings.mlr.press/v37/kusnerb15.html>.
- T. Lin, N. Ho, and M. I. Jordan. On the Efficiency of Entropic Regularized Algorithms for Optimal Transport. *Journal of Machine Learning Research*, 23(137):1–42, 2022. URL <http://jmlr.org/papers/v23/20-277.html>.
- E. C. Meng, T. D. Goddard, E. F. Pettersen, G. S. Couch, Z. J. Pearson, J. H. Morris, and T. E. Ferrin. UCSF ChimeraX: Tools for structure building and analysis. *Protein Science*, 32(11):e4792, 2023. ISSN 1469-896X. doi:[10.1002/pro.4792](https://doi.org/10.1002/pro.4792).
- Q. Mérigot. A Multiscale Approach to Optimal Transport. *Computer Graphics Forum*, 30(5): 1583–1592, Aug. 2011. ISSN 01677055. doi:[10.1111/j.1467-8659.2011.02032.x](https://doi.org/10.1111/j.1467-8659.2011.02032.x).
- E. F. Montesuma, F. M. N. Mboula, and A. Souloumiac. Recent Advances in Optimal Transport for Machine Learning. *IEEE Transactions on Pattern Analysis and Machine Intelligence*, 47(02): 1161–1180, Feb. 2025. ISSN 0162-8828. doi:[10.1109/TPAMI.2024.3489030](https://doi.org/10.1109/TPAMI.2024.3489030).
- T. H. D. Nguyen, W. P. Galej, X.-c. Bai, C. Oubridge, A. J. Newman, S. H. W. Scheres, and K. Nagai. Cryo-EM structure of the yeast U4/U6.U5 tri-snRNP at 3.7 Å resolution. *Nature*, 530(7590): 298–302, Feb. 2016. ISSN 1476-4687. doi:[10.1038/nature16940](https://doi.org/10.1038/nature16940).
- G. Peyré and M. Cuturi. Computational Optimal Transport: With Applications to Data Science. *Foundations and Trends® in Machine Learning*, 11(5-6):355–607, 2019. ISSN 1935-8237, 1935-8245. doi:[10.1561/22000000073](https://doi.org/10.1561/22000000073).
- R. Rao, A. Moscovich, and A. Singer. Wasserstein K-Means for Clustering Tomographic Projections. In *Machine Learning for Structural Biology Workshop, Neural Information Processing Systems (NeurIPS)*, pages 1–12, 2020. URL https://www.mlsb.io/papers/MLSB2020_Wasserstein_K-Means_for_Clustering.pdf.
- A. T. Riahi, G. Woollard, F. Poitevin, A. Condon, and K. D. Duc. AlignOT: An Optimal Transport Based Algorithm for Fast 3D Alignment With Applications to Cryogenic Electron Microscopy Density Maps. *IEEE/ACM Transactions on Computational Biology and Bioinformatics*, 20(6): 3842–3850, Nov. 2023. ISSN 1557-9964. doi:[10.1109/TCBB.2023.3327633](https://doi.org/10.1109/TCBB.2023.3327633).
- G. Schiebinger, J. Shu, M. Tabaka, B. Cleary, V. Subramanian, A. Solomon, J. Gould, S. Liu, S. Lin, P. Berube, L. Lee, J. Chen, J. Brumbaugh, P. Rigollet, K. Hochedlinger, R. Jaenisch, A. Regev, and E. S. Lander. Optimal-Transport Analysis of Single-Cell Gene Expression Identifies Developmental Trajectories in Reprogramming. *Cell*, 176(4):928–943.e22, Feb. 2019. ISSN 1097-4172. doi:[10.1016/j.cell.2019.01.006](https://doi.org/10.1016/j.cell.2019.01.006).
- J. Schrieber, D. Schuhmacher, and C. Gottschlich. DOTmark – A Benchmark for Discrete Optimal Transport. *IEEE Access*, 5:271–282, 2017. ISSN 2169-3536. doi:[10.1109/ACCESS.2016.2639065](https://doi.org/10.1109/ACCESS.2016.2639065).
- S. Shirdhonkar and D. W. Jacobs. Approximate earth mover’s distance in linear time. In *2008 IEEE Conference on Computer Vision and Pattern Recognition*, pages 1–8, June 2008. doi:[10.1109/CVPR.2008.4587662](https://doi.org/10.1109/CVPR.2008.4587662).

- A. Singer and R. Yang. Alignment of density maps in Wasserstein distance. *Biological Imaging*, 4:e5, Jan. 2024. ISSN 2633-903X. doi:[10.1017/S2633903X24000059](https://doi.org/10.1017/S2633903X24000059).
- J. Solomon, F. de Goes, G. Peyré, M. Cuturi, A. Butscher, A. Nguyen, T. Du, and L. Guibas. Convolutional Wasserstein Distances: Efficient Optimal Transportation on Geometric Domains. *ACM Transactions on Graphics*, 34(4):66:1–66:11, 2015. doi:[10.1145/2766963](https://doi.org/10.1145/2766963).
- S. Stagnoli, F. Peccati, S. R. Connell, A. Martinez-Castillo, D. Charro, O. Millet, C. Bruzzone, A. Palazon, A. Ardá, J. Jiménez-Barbero, J. Ereño-Orbea, N. G. A. Abrescia, and G. Jiménez-Osés. Assessing the Mobility of Severe Acute Respiratory Syndrome Coronavirus-2 Spike Protein Glycans by Structural and Computational Methods. *Frontiers in Microbiology*, 13, Apr. 2022. ISSN 1664-302X. doi:[10.3389/fmicb.2022.870938](https://doi.org/10.3389/fmicb.2022.870938).
- C. Villani. *Optimal Transport, Old and New*, volume 338 of *Grundlehren Der Mathematischen Wissenschaften*. Springer, Berlin, Heidelberg, 2009. ISBN 978-3-540-71050-9. doi:[10.1007/978-3-540-71050-9](https://doi.org/10.1007/978-3-540-71050-9).
- W. Wong, X.-c. Bai, A. Brown, I. S. Fernandez, E. Hanssen, M. Condrón, Y. H. Tan, J. Baum, and S. H. Scheres. Cryo-EM structure of the Plasmodium falciparum 80S ribosome bound to the anti-protozoan drug emetine. *eLife*, 3:e03080, June 2014. ISSN 2050-084X. doi:[10.7554/eLife.03080](https://doi.org/10.7554/eLife.03080).
- G. Wright, J. Andén, V. Bansal, J. Xia, C. Langfield, J. Carmichael, K. Sowattanangkul, R. Brook, Y. Shi, A. Heimowitz, G. Pragier, I. Sason, A. Moscovich, Y. Shkolnisky, and A. Singer. ComputationalCryoEM/ASPIRE-Python: V0.13.2. Zenodo, Mar. 2025.
- wwPDB Consortium. EMDb—the Electron Microscopy Data Bank. *Nucleic Acids Research*, 52(D1):D456–D465, Jan. 2024. ISSN 0305-1048. doi:[10.1093/nar/gkad1019](https://doi.org/10.1093/nar/gkad1019).

A Algorithms

Lower-bound based on entropic regularization described in Section 3.1. This method simply runs the iterative Sinkhorn algorithm and then returns the unregularized cost term of the dual solution to the entropic regularization problem.

Algorithm 1 Regularization-Based Lower Bound

Require: $\mu, \nu \in \Sigma_{N^d}$ on $\mathcal{X} = [N]^d$, $p \geq 1, \varepsilon > 0, \xi > 0$ and metric ρ .

$$C \leftarrow \{\rho(x_i, y_j)^p\}_{ij}$$

$$K \leftarrow \exp\left(-\frac{C}{\varepsilon}\right)$$

$$\text{Initialize } \mathbf{f} \leftarrow \mathbf{0}_n, \mathbf{g} \leftarrow \mathbf{0}_m$$

$$\text{Initialize } \mathbf{b} \leftarrow \exp\left(\frac{\mathbf{g}}{\varepsilon}\right)$$

repeat

$$\mathbf{a} \leftarrow \mu \odot (K\mathbf{b})$$

$$\mathbf{f} \leftarrow \varepsilon \log \mathbf{a}$$

$$\mathbf{b} \leftarrow \nu \odot (K^\top \mathbf{a})$$

$$\mathbf{g} \leftarrow \varepsilon \log \mathbf{b}$$

$$\text{until } \|\mathbf{a} \odot K\mathbf{b} - \mu\|_1 + \|\nu - \mathbf{b} \odot K^\top \mathbf{a}\|_1 < \xi$$

$$\text{return } (\langle \mathbf{f}, \mu \rangle + \langle \mathbf{g}, \nu \rangle)^{\frac{1}{p}}$$

Algorithm for entropic regularization-based upper bound described in Section 3.1, using the unregularized term of the primal solution to the entropic regularization problem, with weighted total variation marginal corrections.

Algorithm 2 Regularization-Based Upper Bound

Require: $\mu, \nu \in \Sigma_{N^d}$ on $\mathcal{X} = [N]^d$, $p \geq 1, \varepsilon > 0, \xi > 0$ and metric ρ .

$$C \leftarrow \{\rho(x_i, y_j)^p\}_{ij}$$

$$K \leftarrow \exp\left(-\frac{C}{\varepsilon}\right)$$

$$\text{Initialize } \mathbf{b} \leftarrow \mathbf{1}_{N^d}$$

repeat

$$\mathbf{a} \leftarrow \mu \odot K\mathbf{b}$$

$$\mathbf{b} \leftarrow \nu \odot K^\top \mathbf{a}$$

$$\hat{\mu} \leftarrow \mathbf{a} \odot (K\mathbf{b})$$

$$\hat{\nu} \leftarrow \mathbf{b} \odot (K^\top \mathbf{a})$$

$$\text{until } \|\hat{\mu} - \mu\|_1 + \|\nu - \hat{\nu}\|_1 < \xi$$

$$\hat{\pi}_\varepsilon \leftarrow \text{diag}(\mathbf{a})K \text{diag}(\mathbf{b})$$

$$\bar{x} \leftarrow \text{mean}(\mathcal{X})$$

$$\mathbf{w} \leftarrow \{\rho(\bar{x}, x_i)^p\}_i$$

$$\Delta_{\hat{\mu}} \leftarrow 2^{1-\frac{1}{p}} \langle \mathbf{w}, |\hat{\mu} - \mu| \rangle^{\frac{1}{p}}$$

$$\Delta_{\hat{\nu}} \leftarrow 2^{1-\frac{1}{p}} \langle \mathbf{w}, |\nu - \hat{\nu}| \rangle^{\frac{1}{p}}$$

$$\text{return } \langle \hat{\pi}_\varepsilon, C \rangle^{\frac{1}{p}} + \Delta_{\hat{\mu}} + \Delta_{\hat{\nu}}$$

Algorithm for quantization-based upper bound described in Section 3.2, using coarse cost weighted by the trivial coupling.

Algorithm 3 Weighted-Cost Upper Bound

Require: $\mu, \nu \in \Sigma_{N^d}$ on $\mathcal{X} = [N]^d$, $p \geq 1, \kappa \in \mathbb{N}$ and metric ρ .

$$\tilde{\mu} \leftarrow \text{SumPool}(\mu; \kappa)$$

$$\tilde{\nu} \leftarrow \text{SumPool}(\nu; \kappa)$$

$$\bar{C}_{k\ell} \leftarrow \left\{ \frac{1}{\tilde{\mu}_k \tilde{\nu}_\ell} \sum_{\substack{x \in X_k \\ y \in Y_\ell}} \rho(x, y)^p \mu(x) \nu(y) \right\}_{k\ell}$$

$$\text{Solve } L_{\bar{C}} \leftarrow \min_{\tilde{\pi} \in \Pi(\tilde{\mu}, \tilde{\nu})} \langle \tilde{\pi}, \bar{C} \rangle$$

$$\text{return } L_{\bar{C}}^{\frac{1}{p}}$$

Algorithm for bi-level quantization-based upper bound described in Section 3.4, using nearest-neighbor upscaling of the optimal coarse coupling, iterative proportional fitting of the marginals (i.e. Sinkhorn iterations), with weighted total variation marginal corrections.

Algorithm 4 Upscaling Upper Bound

Require: $\mu, \nu \in \Sigma_{N^d}$ on $\mathcal{X} = [N]^d$, $p \geq 1$, $\kappa \in \mathbb{N}$, $\xi > 0$ and metric ρ .

$\tilde{\mathcal{X}} \leftarrow \text{AvgPool}(\mathcal{X}; \kappa)$
 $\tilde{\mu} \leftarrow \text{SumPool}(\mu; \kappa)$
 $\tilde{\nu} \leftarrow \text{SumPool}(\nu; \kappa)$
 $\tilde{C} \leftarrow \{\rho(\tilde{x}_k, \tilde{x}_\ell)^p\}_{k\ell}$
 Solve $\tilde{\pi}^* \leftarrow \arg \min_{\tilde{\pi} \in \Pi(\tilde{\mu}, \tilde{\nu})} \langle \tilde{\pi}, \tilde{C} \rangle$
 \triangleright **Up-scaled coupling**
 $\tilde{\mathbf{P}}^* \leftarrow \text{reshape}(\tilde{\pi}^*; n)$ \triangleright Reshape as tensor
 $\mathbf{K} \leftarrow \{\kappa^{-2d}\}_{t \in [n]^{2d}}$
 $\hat{\mathbf{P}} \leftarrow \tilde{\mathbf{P}}^* \otimes \mathbf{K}$ \triangleright Upscaling
 $\hat{\pi} \leftarrow \text{reshape}^{-1}(\hat{\mathbf{P}}; N)$
 \triangleright **Iterative proportional fitting**
 Initialize $\mathbf{b} \leftarrow \mathbf{1}_{N^d}$
repeat
 $\mathbf{a} \leftarrow \mu \otimes \hat{\pi} \mathbf{b}$
 $\mathbf{b} \leftarrow \nu \otimes \hat{\pi}^\top \mathbf{a}$
 $\hat{\mu} \leftarrow \mathbf{a} \odot (\hat{\pi} \mathbf{b})$
 $\hat{\nu} \leftarrow \mathbf{b} \odot (\hat{\pi}^\top \mathbf{a})$
until $\|\hat{\mu} - \mu\|_1 + \|\nu - \hat{\nu}\|_1 < \xi$
 \triangleright **Upper bound**
 $\widehat{\mathcal{W}}_p \leftarrow \left(\sum_{(i,j) \in \text{supp}(\hat{\pi})} a_i \hat{\pi}_{ij} b_j \rho(x_i, x_j)^p \right)^{\frac{1}{p}}$
 $\bar{x} \leftarrow \text{mean}(\mathcal{X})$
 $\mathbf{w} \leftarrow \{\rho(\bar{x}, x_i)^p\}_i$
 $\Delta_{\hat{\mu}} \leftarrow 2^{1-\frac{1}{p}} \langle \mathbf{w}, |\hat{\mu} - \mu| \rangle^{\frac{1}{p}}$
 $\Delta_{\hat{\nu}} \leftarrow 2^{1-\frac{1}{p}} \langle \mathbf{w}, |\nu - \hat{\nu}| \rangle^{\frac{1}{p}}$
return $\widehat{\mathcal{W}}_p + \Delta_{\hat{\mu}} + \Delta_{\hat{\nu}}$

Algorithm for bi-level quantization-based lower bound described in Section 3.5, using interpolation for upscaling the optimal coarse dual potentials, and c-transform to achieve optimized admissible dual potentials pair.

Algorithm 5 Upscaling Lower Bound

Require: $\mu, \nu \in \Sigma_{N^d}$ on $\mathcal{X} = [N]^d$, $p \geq 1$, $\kappa \in \mathbb{N}$ and metric ρ .

$\tilde{\mathcal{X}} \leftarrow \text{AvgPool}(\mathcal{X}; \kappa)$
 $\tilde{\mu} \leftarrow \text{SumPool}(\mu; \kappa)$
 $\tilde{\nu} \leftarrow \text{SumPool}(\nu; \kappa)$
 $\tilde{C} \leftarrow \{\rho(\tilde{x}_k, \tilde{x}_\ell)^p\}_{k\ell}$
 Solve $(\tilde{\mathbf{f}}^*, \tilde{\mathbf{g}}^*) \leftarrow \arg \max_{(\tilde{\mathbf{f}}, \tilde{\mathbf{g}}) \in \mathcal{R}(\tilde{C})} \langle \tilde{\mathbf{f}}, \tilde{\mu} \rangle + \langle \tilde{\mathbf{g}}, \tilde{\nu} \rangle$
 $\hat{\mathbf{f}} \leftarrow \{R_{\tilde{\mathbf{f}}, \tilde{\mathcal{X}}}(x_i)\}_{i \in [N^d]}$
 $\mathbf{g} \leftarrow \left\{ \min_i \rho(x_i, x_j)^p - \hat{f}_i \right\}_j$
 $\mathbf{f} \leftarrow \left\{ \min_j \rho(x_i, x_j)^p - g_j \right\}_i$
return $(\langle \mathbf{f}, \mu \rangle + \langle \mathbf{g}, \nu \rangle)^{\frac{1}{p}}$

Class	p	Upper Bounds						Lower Bounds					
		Weighted-Cost		Primal Upscaling		Entropic Regularization		Dual Upscaling		Min-Cost		Entropic Regularization	
		κ_2	κ_4	κ_2	κ_4	ε_1	ε_4	κ_2	κ_4	κ_2	κ_4	ε_1	ε_4
Classic Images	1	4.4%	0.3%	5.0%	0.3%	19.8%	16.0%	4.9%	0.2%	4.7%	0.3%	17.6%	18.7%
		$\pm 2.1\%$	$\pm 0.2\%$	$\pm 2.6\%$	$\pm 0.4\%$	$\pm 10.1\%$	$\pm 11.2\%$	$\pm 2.6\%$	$\pm 0.1\%$	$\pm 2.3\%$	$\pm 0.1\%$	$\pm 7.8\%$	$\pm 13.3\%$
Microscopy	2	6.1%	0.4%	6.1%	0.3%	7.9%	1.3%	6.1%	0.3%	6.1%	0.3%	12.3%	1.3%
		$\pm 3.1\%$	$\pm 0.1\%$	$\pm 3.0\%$	$\pm 0.1\%$	$\pm 6.6\%$	$\pm 0.5\%$	$\pm 3.0\%$	$\pm 0.1\%$	$\pm 2.9\%$	$\pm 0.1\%$	$\pm 10.4\%$	$\pm 0.6\%$
Shapes	1	16.7%	2.3%	20.7%	6.6%	128.0%	90.7%	14.4%	2.2%	15.7%	1.9%	120.8%	86.9%
		$\pm 5.6\%$	$\pm 1.4\%$	$\pm 9.6\%$	$\pm 10.6\%$	$\pm 68.3\%$	$\pm 79.2\%$	$\pm 5.0\%$	$\pm 1.2\%$	$\pm 4.8\%$	$\pm 1.0\%$	$\pm 57.2\%$	$\pm 81.3\%$
	2	15.4%	1.9%	17.4%	3.0%	75.6%	7.7%	15.6%	2.0%	14.9%	1.7%	99.9%	8.1%
		$\pm 5.2\%$	$\pm 1.2\%$	$\pm 5.9\%$	$\pm 3.4\%$	$\pm 51.3\%$	$\pm 4.9\%$	$\pm 5.1\%$	$\pm 1.3\%$	$\pm 5.0\%$	$\pm 1.0\%$	$\pm 72.8\%$	$\pm 5.5\%$
	1	10.2%	1.9%	15.1%	10.8%	172.9%	68.8%	7.8%	1.5%	8.5%	1.4%	163.6%	77.0%
		$\pm 3.6\%$	$\pm 1.7\%$	$\pm 8.9\%$	$\pm 11.9\%$	$\pm 99.0\%$	$\pm 72.7\%$	$\pm 2.0\%$	$\pm 0.7\%$	$\pm 2.4\%$	$\pm 1.2\%$	$\pm 88.8\%$	$\pm 77.6\%$
	2	7.9%	1.5%	9.6%	4.2%	39.5%	6.0%	7.4%	1.2%	7.3%	1.0%	56.2%	5.7%
		$\pm 3.8\%$	$\pm 1.8\%$	$\pm 5.6\%$	$\pm 6.4\%$	$\pm 45.0\%$	$\pm 11.6\%$	$\pm 2.6\%$	$\pm 0.6\%$	$\pm 3.0\%$	$\pm 1.4\%$	$\pm 69.1\%$	$\pm 11.8\%$

Table 4: Computational time comparison of different methods showing the mean \pm standard deviation of the relative computation time compared to exact OT solver. Each method is evaluated at different fidelity level $\kappa_2 = 2$ and $\kappa_4 = 4$ and different values of $\varepsilon_1 = 1 \cdot 10^{-3}N^p$ and $\varepsilon_4 = 4 \cdot 10^{-3}N^p$.

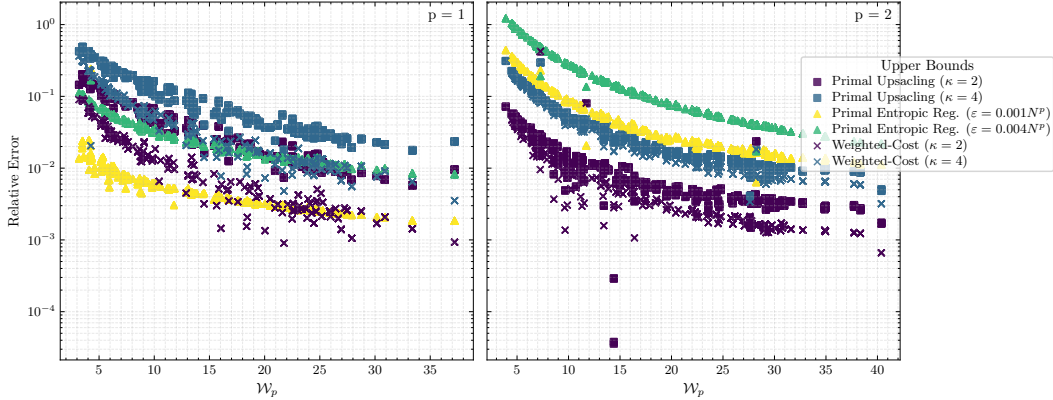


Figure 5: Accuracy of Wasserstein Upper Bounds

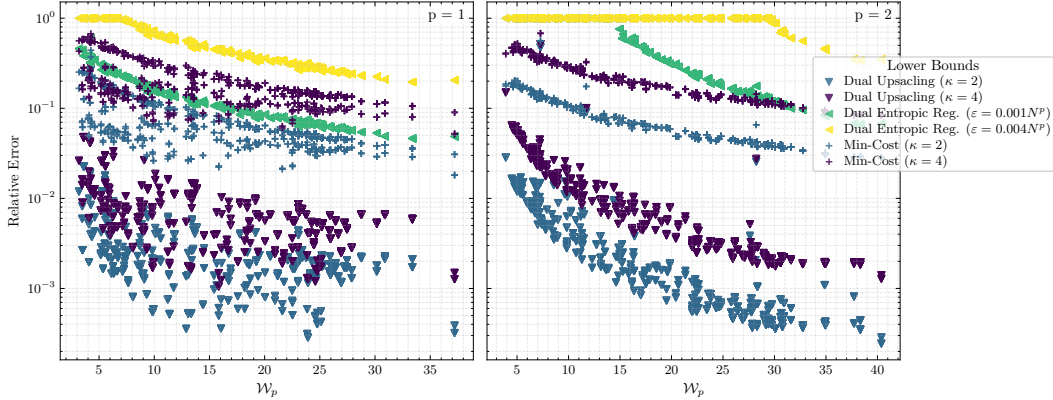


Figure 6: Accuracy of Wasserstein Lower Bounds. Negative-valued bounds are clipped to 0, evaluating as 100% relative error.

B Experiments

B.1 DOTmark

In this section we present additional figures and results evaluating the proposed Wasserstein bounds on the discrete optimal transport benchmark (DOTMark) [Schrieber et al., 2017] presented in the main text. The computational speed up of the proposed methods compared to the exact OT solver are summarized in Table 4. The results show that the quantization methods achieve the most significant speed ups. Notably, the dual upscaling method at $\kappa = 4$ are calculated in 0.2-2.2% of the time, while making almost no sacrifice in accuracy. Maintaining no more than 2.4% average error.

The relative accuracy of the proposed methods exponentially improves for large values of the exact Wasserstein distance as evident in Figures 5 and 6. Negative-valued lower bounds are trivially clipped to 0, when evaluate in the benchmark.

B.2 EMDB

The Electron Microscopy Data Bank (EMDB) [wwPDB Consortium, 2024] is a repository of volumetric density maps that contains many interesting molecules that were reconstructed from cryogenic electron microscopy (cryo-EM) experiments. These reconstructions are estimates of the 3D electric potential at every point in the molecule. For our 3D experiments, we downloaded and processed four maps of famous molecules, detailed in Table 5 using the ASPIRE package [Wright et al., 2025]. In Figure 4 you can see 3D renderings of these molecules that we generated using UCSF ChimeraX [Meng et al., 2023]. The volumetric maps were downloaded from EMDB, masked inside a spherical region of radius 128 pixels, rotated around the Z axis in increments of 20 degrees and downscaled to $16 \times 16 \times 16$ voxels. The computational speed up is summarized in Table 6, showing that even at $\kappa = 2$ the quantization methods provide substantial speedups. Figure 8 shows the Wasserstein metrics and bounds between the 3D density map of the molecule in its base orientation and its rotations around the Z axis. The exact Wasserstein metric is shown as the thick black line with upper and lower bounds next to it using the various markers.

The quantization-based methods dominate in accuracy for the lower bounds of both $p \in \{1, 2\}$, whereas for the upper bounds of the Wasserstein-1 metric, the upper bound based on entropic regularization with $\varepsilon = 0.001N^p$ achieves the best accuracy, although at a significant computational cost. The triangular symmetry of EMDB-14621 (SARS-CoV-2 spike protein) and EMDB-2484 (Trimeric HIV-1 envelope glycoprotein) seen in Figure 8 are easily detectable as the dips at 120° rotation angle.

Table 5: Selected cryo-EM structures from the Electron Microscopy Data Bank (EMDB).

Name	EMDB ID	Description
Ribosome	EMD-2660	Ribosome of the Plasmodium falciparum parasite which causes malaria in humans [Wong et al., 2014]
SARS-CoV-2	EMD-14621	SARS-CoV-2 spike protein [Stagnoli et al., 2022]
Yeast	EMD-8012	Yeast spliceosome [Nguyen et al., 2016]
HIV	EMD-2484	HIV-1 trimeric spike pre-fusion [Bartesaghi et al., 2013]

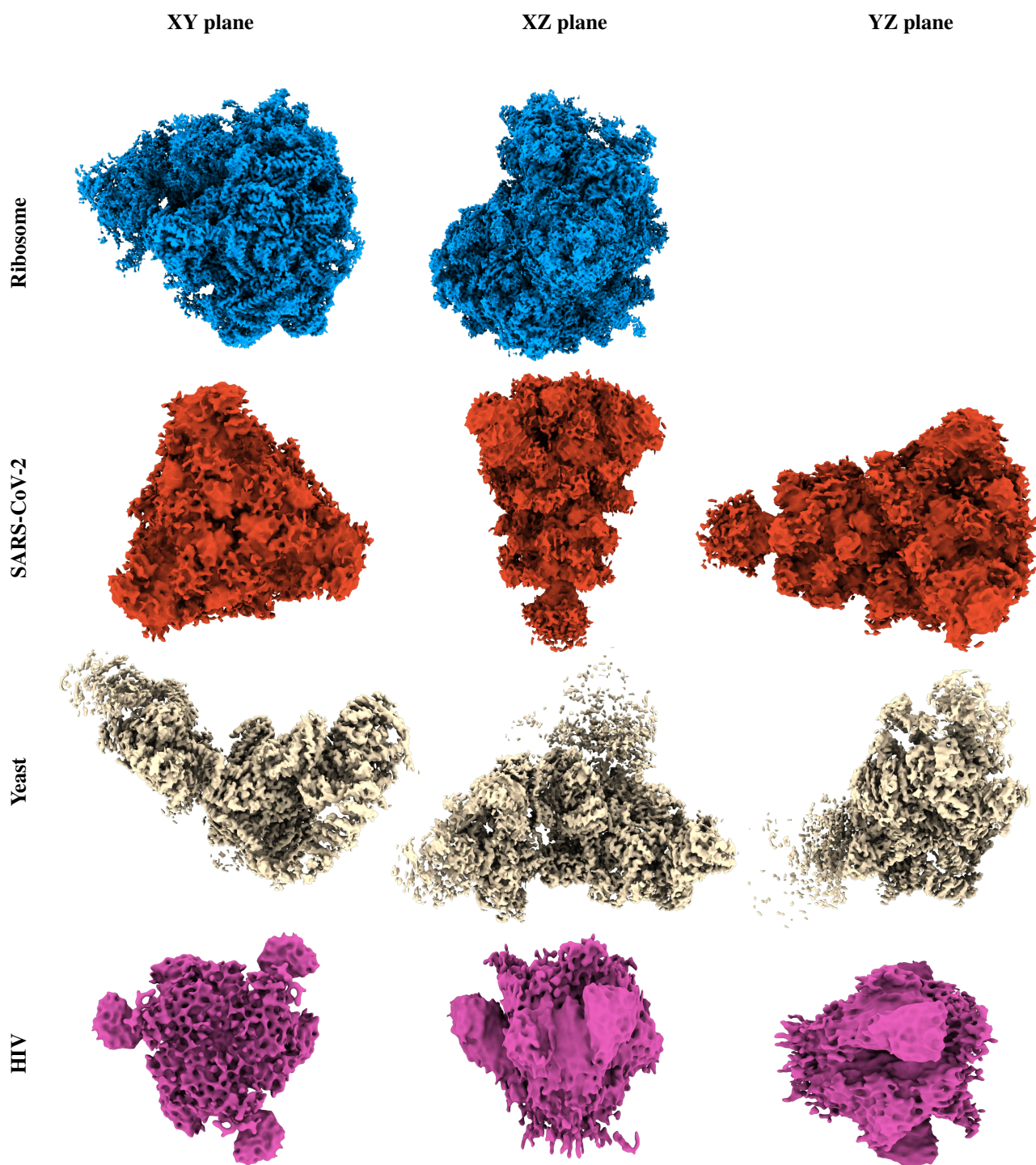


Figure 7: Isosurfaces of 3D molecular densities from the Electron Microscopy Data Bank (EMDB). In our experiments, the molecules on the left are rotated around the Z axis, which corresponds to the depth direction here. The middle and right columns show the same molecules rotated by 90 degrees around the X and Y axis (respectively).

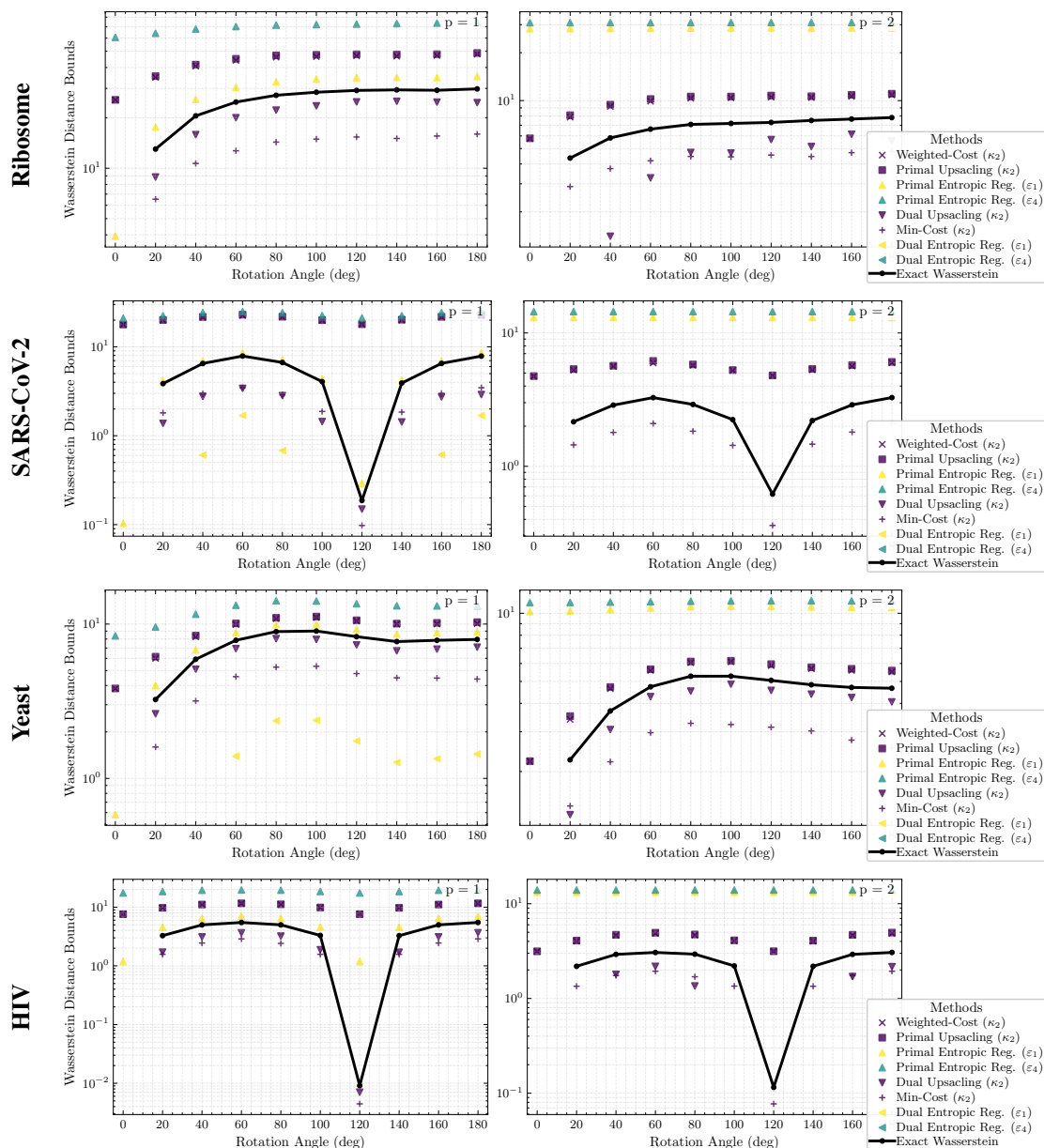


Figure 8: Wasserstein- p metric and bounds between rotated 3D density maps of the molecules described in Table 5. From top to bottom: **Ribosome**, **SARS-CoV-2**, **Yeast**, **HIV**. The thick black line is the exact Wasserstein metric between the molecule and its rotated self, as a function of the rotation angle. The various upper and lower bounds are shown as different color markers. Note the drop around 120 degrees for the SARS-CoV-2 and HIV-1 spikes due to their 3-fold symmetry.

Table 6: Relative computation time compared to exact OT solver of $16 \times 16 \times 16$ downscaled EMDB density maps. Results show mean and standard deviation across rotation angles. Lower is better.

Molecule	p	Upper Bounds				Lower Bounds			
		Weighted-	Primal	Entropic		Dual	Min-	Entropic	
		Cost	Upscaling	Regularization	Regularization	Upscaling	Cost	Regularization	Regularization
		κ_2	κ_2	ε_1	ε_4	κ_2	κ_2	ε_1	ε_4
Ribosome	1	3.7% $\pm 3.2\%$	175.6% $\pm 56.2\%$	156.2% $\pm 111.3\%$	155.8% $\pm 111.1\%$	74.5% $\pm 21.8\%$	3.5% $\pm 3.0\%$	154.1% $\pm 109.8\%$	154.1% $\pm 109.7\%$
	2	12.4% $\pm 3.7\%$	178.1% $\pm 226.5\%$	569.8% $\pm 252.8\%$	570.2% $\pm 252.3\%$	12.2% $\pm 3.6\%$	12.5% $\pm 5.0\%$	563.2% $\pm 249.8\%$	563.6% $\pm 249.6\%$
SARS-CoV-2	1	11.4% $\pm 26.7\%$	164.6% $\pm 96.4\%$	69.1% $\pm 4.7\%$	62.7% $\pm 15.1\%$	69.9% $\pm 35.7\%$	2.2% $\pm 0.3\%$	61.4% $\pm 14.0\%$	61.2% $\pm 14.8\%$
	2	19.7% $\pm 3.5\%$	350.5% $\pm 421.2\%$	850.9% $\pm 895.4\%$	658.8% $\pm 303.0\%$	77.9% $\pm 184.2\%$	19.0% $\pm 5.7\%$	642.5% $\pm 295.5\%$	641.6% $\pm 294.0\%$
Yeast	1	4.8% $\pm 4.9\%$	295.4% $\pm 379.0\%$	20.8% $\pm 31.2\%$	3.1% $\pm 3.5\%$	127.5% $\pm 153.4\%$	3.3% $\pm 3.3\%$	5.6% $\pm 4.6\%$	0.9% $\pm 0.9\%$
	2	12.7% $\pm 0.7\%$	172.2% $\pm 69.3\%$	919.4% $\pm 497.3\%$	828.9% $\pm 215.6\%$	13.3% $\pm 1.0\%$	11.6% $\pm 0.7\%$	820.4% $\pm 213.8\%$	819.7% $\pm 212.5\%$
HIV	1	10.4% $\pm 23.6\%$	243.1% $\pm 215.3\%$	163.1% $\pm 127.3\%$	163.0% $\pm 127.1\%$	99.6% $\pm 89.8\%$	2.9% $\pm 2.7\%$	161.1% $\pm 125.8\%$	161.1% $\pm 125.8\%$
	2	40.7% $\pm 97.7\%$	198.2% $\pm 255.3\%$	603.9% $\pm 252.2\%$	603.9% $\pm 252.0\%$	45.6% $\pm 114.3\%$	40.4% $\pm 99.0\%$	597.0% $\pm 249.3\%$	597.0% $\pm 249.3\%$

C Proofs

C.1 Weighted total variation correction terms

Proof of Lemma 3.2. Using the triangle inequality for the Wasserstein metric, we can write

$$\mathcal{W}_p(\mu, \nu) \leq \mathcal{W}_p(\mu, \hat{\mu}) + \mathcal{W}_p(\hat{\mu}, \hat{\nu}) + \mathcal{W}_p(\hat{\nu}, \nu) \quad (29)$$

controlling for each element separately, we have

$$\mathcal{W}_p(\mu, \hat{\mu}) \leq \mathcal{TV}_p^w(\hat{\mu}, \mu) \quad \text{and} \quad \mathcal{W}_p(\hat{\nu}, \nu) \leq \mathcal{TV}_p^w(\nu, \hat{\nu}) \quad (30)$$

by the property of weighted total variation, and

$$\mathcal{W}_p(\hat{\mu}, \hat{\nu}) = \left(\min_{\pi \in \Pi(\hat{\mu}, \hat{\nu})} \langle \pi, C \rangle \right)^{\frac{1}{p}} \leq \langle \hat{\pi}, C \rangle^{\frac{1}{p}} \quad (31)$$

by evaluating the transport cost using a coupling in the problem's original space. \square

Proof of Proposition 3.3. Consider the definition of weighted total variation,

$$\begin{aligned} & \mathcal{TV}_p(\hat{\mu}, \mu; w) + \mathcal{TV}_p(\nu, \hat{\nu}; w) & (32) \\ &= 2^{1-\frac{1}{p}} \langle w, |\hat{\mu} - \mu| \rangle^{\frac{1}{p}} + 2^{1-\frac{1}{p}} \langle w, |\nu - \hat{\nu}| \rangle^{\frac{1}{p}} \\ &= 2^{1-\frac{1}{p}} \left(\left(\sum \rho(\bar{x}, x)^p |\hat{\mu}_x - \mu_x| \right)^{\frac{1}{p}} + \left(\sum \rho(\bar{x}, x)^p |\nu_x - \hat{\nu}_x| \right)^{\frac{1}{p}} \right) \\ &\leq 2^{1-\frac{1}{p}} \left(r \|\hat{\mu} - \mu\|_1^{\frac{1}{p}} + r \|\nu - \hat{\nu}\|_1^{\frac{1}{p}} \right) & \text{bounding radius} \\ &\leq 2^{2-\frac{2}{p}} (\|\hat{\mu} - \mu\|_1 + \|\nu - \hat{\nu}\|_1)^{\frac{1}{p}} r & \text{Jensen's inequality} \\ &< 2^{2-\frac{2}{p}} \xi^{\frac{1}{p}} r & \text{convergence criteria} \end{aligned}$$

\square

C.2 Proof of Theorem 3.4

First, let us consider the following lemma discussing a coupling constructed ad hoc using coarsened measures.

Lemma C.1. *Let μ, ν measures with set of admissible couplings $\Pi(\mu, \nu)$, the trivial coupling π_{\otimes} , and $\tilde{\mu}$ and $\tilde{\nu}$ the respective coarsened measures. For any coupling $\tilde{\pi} \in \Pi(\tilde{\mu}, \tilde{\nu})$, the measure on the product space $\mathcal{X} \times \mathcal{Y}$*

$$\pi_{\tilde{\pi}}(x, y) := \frac{\tilde{\pi}_{k_{\mathbb{X}}(x)\ell_{\mathbb{Y}}(y)}}{\mu(X_{k_{\mathbb{X}}(x)})\nu(Y_{\ell_{\mathbb{Y}}(y)})}\pi_{\otimes}(x, y) \quad (33)$$

is an admissible coupling $\pi_{\tilde{\pi}} \in \Pi(\mu, \nu)$, where the coarsening inverse index functions $k_{\mathbb{X}}(x), \ell_{\mathbb{Y}}(y)$ are defined as $k_{\mathbb{X}}(x) := \{k : x \in X_k\}, \ell_{\mathbb{Y}}(y) := \{\ell : y \in Y_{\ell}\}$.

Proof of Lemma C.1. Following Definition 1.1 (Coupling) from [Villani, 2009], one can show $\pi_{\tilde{\pi}}(x, y)$ Equation (33) is admissible. For φ, ψ be any integrable measurable functions on \mathcal{X}, \mathcal{Y} respectively, than $\pi_{\tilde{\pi}}(x, y)$ admits

$$\begin{aligned} & \int_{\mathcal{X} \times \mathcal{Y}} (\varphi(x) + \psi(y)) d\pi_{\tilde{\pi}}(x, y) \quad (34) \\ &= \sum_{k, \ell} \int_{X_k \times Y_{\ell}} (\varphi(x) + \psi(y)) d\pi_{\tilde{\pi}}(x, y) \\ &= \sum_{k, \ell} \int_{X_k \times Y_{\ell}} (\varphi(x) + \psi(y)) \frac{\mathbf{\Pi}_{k\ell}}{\mu(X_k)\nu(Y_{\ell})} d\mu(x)d\nu(y) \quad \text{plug-in coupling's definition} \\ &= \sum_{k, \ell} \left(\frac{\tilde{\pi}_{k\ell}}{\mu(X_k)\nu(Y_{\ell})} \int_{X_k \times Y_{\ell}} \varphi(x) d\mu(x)d\nu(y) + \frac{\tilde{\pi}_{k\ell}}{\mu(X_k)\nu(Y_{\ell})} \int_{X_k \times Y_{\ell}} \psi(y) d\mu(x)d\nu(y) \right) \\ &= \sum_{k, \ell} \frac{\tilde{\pi}_{k\ell}}{\mu(X_k)} \int_{X_k} \varphi(x) d\mu(x) + \sum_{k, \ell} \frac{\tilde{\pi}_{k\ell}}{\nu(Y_{\ell})} \int_{Y_{\ell}} \psi(y) d\nu(y) \quad \text{sum over marginals} \\ &= \sum_k \int_{X_k} \varphi(x) d\mu(x) + \sum_{\ell} \int_{Y_{\ell}} \psi(y) d\nu(y) \\ &= \int_{\mathcal{X}} \varphi(x) d\mu(x) + \int_{\mathcal{Y}} \psi(y) d\nu(y) \end{aligned}$$

□

Next, we consider the transport cost of such a coupling.

Lemma C.2. *The transport loss assigned by the cost $c(x, y)$ and a coupling $\pi_{\tilde{\pi}}$ identifies with the coarse transport loss assigned by marginally weighted cost \bar{C} Equation (15) and the coarse coupling $\tilde{\pi}$,*

$$\langle \pi_{\tilde{\pi}}, C \rangle = \langle \tilde{\pi}, \bar{C} \rangle \quad (35)$$

Proof.

$$\begin{aligned}
\langle \pi_{\tilde{\pi}}, C \rangle &= \sum_{i,j} c(x_i, y_j) \pi_{\tilde{\pi}}(x_i, y_j) = \sum_{k,\ell} \sum_{\substack{x \in X_k \\ y \in Y_\ell}} c(x, y) \pi_{\tilde{\pi}}(x, y) \\
&= \sum_{k,\ell} \sum_{\substack{x \in X_k \\ y \in Y_\ell}} c(x, y) \frac{\tilde{\pi}_{k\ell}}{\mu(X_k) \nu(Y_\ell)} \pi_{\otimes}(x, y) \\
&= \sum_{k,\ell} \frac{1}{\mu(X_k) \nu(Y_\ell)} \sum_{\substack{x \in X_k \\ y \in Y_\ell}} c(x, y) \mu(x) \nu(y) \tilde{\pi}_{k\ell} \\
&= \sum_{k,\ell} \bar{C}_{k\ell} \tilde{\pi}_{k\ell} = \langle \tilde{\pi}, \bar{C} \rangle
\end{aligned} \tag{36}$$

□

Finally, we can write

Proof of Theorem 3.4. Based on admissibility of $\pi_{\tilde{\pi}}$ shown in Lemma C.1 the transport cost

$$\langle \pi_{\tilde{\pi}}, C \rangle \geq L_C(\mu, \nu), \quad \forall \tilde{\pi} \in \Pi(\tilde{\mu}, \tilde{\nu}). \tag{37}$$

In particular, for $\tilde{\pi}^* = \arg \min_{\tilde{\pi} \in \Pi(\tilde{\mu}, \tilde{\nu})} \langle \tilde{\pi}, \bar{C} \rangle$,

$$\langle \tilde{\pi}^*, \bar{C} \rangle = \langle \pi_{\tilde{\pi}^*}, C \rangle \geq L_C(\mu, \nu) \tag{38}$$

by the identity shown in Lemma C.2.

□

C.3 Additional proofs

Proof of Theorem 3.5. Consider

$$\pi^* = \arg \min_{\pi \in \Pi(\mu, \nu)} \langle \pi, C \rangle \tag{39}$$

and coarsening of the optimal coupling

$$\hat{\pi}_{k\ell}^* := \sum_{\substack{x \in X_k \\ y \in Y_\ell}} \pi^*(x, y) \tag{40}$$

such that,

$$\begin{aligned}
L_C(\mu, \nu) &= \langle \pi^*, C \rangle \\
&= \sum_{\substack{x \in \mathcal{X} \\ y \in \mathcal{Y}}} \rho(x, y)^p \pi^*(x, y) \\
&= \sum_{k,\ell} \sum_{\substack{x \in X_k \\ y \in Y_\ell}} \rho(x, y)^p \pi^*(x, y) \\
&\geq \sum_{k,\ell} C_{k\ell}^{\min} \sum_{\substack{x \in X_k \\ y \in Y_\ell}} \pi^*(x, y) \\
&= \langle \hat{\pi}^*, C^{\min} \rangle \\
&\geq \min_{\tilde{\pi} \in \Pi(\tilde{\mu}, \tilde{\nu})} \langle \tilde{\pi}, C^{\min} \rangle \\
&= L_{C^{\min}}(\tilde{\mu}, \tilde{\nu}).
\end{aligned} \tag{41}$$

□

Proof of Lemma 3.6. Let $\tilde{\pi}^* \in \Pi(\tilde{\mu}, \tilde{\nu})$ be the coarse optimal coupling and \mathbf{K} be the positive valued normalized kernel tensor satisfying $\sum_{t \in [\kappa]^{2d}} \mathbf{K}_t = 1$. Recall that $\hat{\mathbf{P}} = \tilde{\mathbf{P}}^* \otimes \mathbf{K}$ and $\hat{\pi}$ is obtained by reshaping $\hat{\mathbf{P}}$.

First, we show that the sum of all elements equals 1:

$$\begin{aligned}
\sum_{i=1}^{N^d} \sum_{j=1}^{N^d} \hat{\pi}_{ij} &= \sum_{t \in [\kappa]^{2d}} \sum_{k=1}^{n^d} \sum_{\ell=1}^{n^d} \tilde{\pi}_{k\ell}^* \mathbf{K}_t \\
&= \sum_{k=1}^{n^d} \sum_{\ell=1}^{n^d} \tilde{\pi}_{k\ell}^* \sum_{t \in [\kappa]^{2d}} \mathbf{K}_t \\
&= \sum_{k=1}^{n^d} \sum_{\ell=1}^{n^d} \tilde{\pi}_{k\ell}^* \cdot 1 = 1
\end{aligned} \tag{42}$$

where the last equality follows from $\tilde{\pi}^*$ being a coupling.

Second, we show that $\hat{\pi}$ is non-negative. Since $\tilde{\pi}^*$ is a coupling, it is non-negative, and \mathbf{K} is a positive-valued kernel, their tensor product $\hat{\mathbf{P}}$ and its reshaped form $\hat{\pi}$ are non-negative.

Thus, $\hat{\pi}$ satisfies all the properties of a coupling measure. \square

D Table of notations

Table 7: Table of Notations

Notation	Category	Description
<i>Sets and Spaces</i>		
\mathbb{R}_+	Set	Non-negative real numbers
$[n]$	Set	Set of integers $\{1, \dots, n\}$
Σ_N	Space	Probability simplex $\{(p_1, \dots, p_N) \in \mathbb{R}_+^N : \sum_i p_i = 1\}$
\mathcal{X}, \mathcal{Y}	Set	Point sets where measures are defined
\mathbb{X}	Set	Set of non-overlapping hypercubes covering the grid
$\tilde{\mathcal{X}}, \tilde{\mathcal{Y}}$	Set	Coarse grids (set of hypercube centers)
X_k, Y_ℓ	Set	Individual hypercubes in the partition
<i>Measures and Vectors</i>		
$\mathbf{0}_n, \mathbf{1}_n$	Vector	All-zeros and all-ones vectors in \mathbb{R}^n , respectively
μ, ν	Measure	Discrete probability measures
$\boldsymbol{\mu}, \boldsymbol{\nu}$	Vector	Vector representations of measures μ, ν
$\tilde{\mu}, \tilde{\nu}$	Measure	Coarsened measures
$\tilde{\boldsymbol{\mu}}, \tilde{\boldsymbol{\nu}}$	Vector	Vector representations of coarsened measures
\mathbf{f}, \mathbf{g}	Vector	Kantorovich potentials
\mathbf{a}, \mathbf{b}	Vector	Sinkhorn scaling vectors
<i>Matrices and Tensors</i>		
C	Matrix	Ground-cost matrix
\tilde{C}	Matrix	Coarse cost matrix (center-based)
\bar{C}	Matrix	Coarse cost matrix (average-based)
π	Matrix	Transport plan (coupling matrix)
π^*	Matrix	Optimal transport coupling
$\tilde{\pi}$	Matrix	Coarse coupling
\mathbf{K}	Tensor	Normalized kernel tensor
<i>Functions and Operations</i>		
ρ	Function	Distance metric
\mathcal{W}_p	Function	Wasserstein- p metric
L_C	Function	Optimal transport cost for ground-cost C
\mathcal{TV}_p^w	Function	Weighted total variation
\otimes	Operation	Tensor product
\odot, \oslash	Operation	Pointwise multiplication, division
$\langle \cdot, \cdot \rangle$	Operation	Standard vector/matrix inner product
<i>Parameters and Constants</i>		
p	Parameter	Order of Wasserstein metric ($p \geq 1$)
κ	Parameter	Scale factor for coarsening
ξ	Parameter	Convergence threshold for fitting
N	Constant	Side length of regular grid
d	Constant	Dimension of the space
n	Constant	Side length of coarse grid ($n = N/\kappa$)
\bar{x}	Constant	Center point of space \mathcal{X}
r	Constant	Radius of space \mathcal{X}
$\Delta_{\tilde{\mu}}, \Delta_{\tilde{\nu}}$	Constant	Marginal weighed total variation corrections
<i>Code</i>		
AvgPool, SumPool	Function	Average/sum pooling layer with identical kernel size and stride
mean	Function	Mean of a set of points
reshape	Function	Cardinality preserving tensor shape transformation